

Anisotropic wetting of ZnO by Bi₂O₃ with and without nanometer-thick surficial amorphous films

Haijun Qian^a, Jian Luo^{a,*}, Yet-Ming Chiang^b

^a School of Materials Science and Engineering, Center of Optical Materials Science and Engineering Technologies (COMSET), Clemson University, Clemson, SC 29634, USA

^b Department of Materials Science and Engineering, Massachusetts Institute of Technology, Cambridge, MA 02139, USA

Received 23 August 2007; received in revised form 16 October 2007; accepted 17 October 2007

Abstract

Anisotropic formation of equilibrium-thickness Bi₂O₃-enriched surficial amorphous films (SAFs) on ZnO has been documented [Luo J, Chiang Y-M. *Acta Mater* 2000;48:4501]. This study further explores anisotropic wetting of ZnO single crystals by Bi₂O₃-rich liquid with and without SAFs. For Bi₂O₃ on the ZnO {11 $\bar{2}$ 0} surfaces wherein nanometer-thick SAFs are present in equilibrium with partial wetting drops, the measured (advancing) contact angle decreases with increasing temperature, but it stabilizes at $\sim 6^\circ$ above $\sim 860^\circ\text{C}$. In contrast, the contact angle is virtually a constant on the {1 $\bar{1}$ 00} surfaces where SAFs are not present. This observation suggests that wetting in the presence of nanoscale SAFs follows a generalized Cahn wetting model. Faceted ridge formation at the triple lines and associated pinning effects are observed. Observation and analysis of unique two-stage isothermal drop receding kinetics show that complete wetting does not occur up to 1050°C and that the receding contact angle is estimated to be $\sim 4^\circ$ via two methods. Quantitative evaluation of a thermodynamic model shows that the observed “residual” contact angle of $\sim 4\text{--}6^\circ$ and the extended SAF stability can be explained on the basis of a significant attractive London dispersion force.

© 2007 Acta Materialia Inc. Published by Elsevier Ltd. All rights reserved.

Keywords: Anisotropy; Equilibrium-thickness; Intergranular films; Surficial amorphous films; Prewetting

1. Introduction

Equilibrium-thickness intergranular films (IGFs) have been widely observed at grain boundaries and hetero-phase interfaces in ceramic materials [1–4], as well as at metal/oxide hetero-interfaces [5–10] and metallic grain boundaries [11,12]. Free-surface counterparts to these IGFs have also been found for Bi₂O₃ on ZnO [13–16], VO_x on TiO₂ [17] and several other oxide systems [9,14,15] (including silicate-based films on Al₂O₃ surfaces partially wetted by anorthite [9]). These are termed surficial amorphous films (SAFs), although partial order generally exists within the films. (At equilibration temperatures, both IGFs and SAFs can be considered as quasi-liquid interfacial films exhibit-

ing partial structural order imposed by adjacent crystals [18].) Like IGFs, these SAFs are impurity-based liquid-like layers that adopt an “equilibrium” thickness on the order of 1 nm as a balance among several attractive and repulsive interfacial forces [13–16,18]. It was proposed [15,16,18,19] that these SAFs and IGFs can alternatively be considered as disordered multilayer adsorbates that form from coupled prewetting [20] and premelting [21–23] transitions.

From the viewpoint of wetting, SAFs and IGFs can be considered in a “moist” regime, existing between the regimes of Langmuir submonolayer adsorption and complete wetting [2,3,15,16,18]. For Bi₂O₃-enriched SAFs on ZnO {11 $\bar{2}$ 0} surfaces [15] (as well as VO_x-enriched SAFs on anatase {101} surfaces [17]), the equilibrium thickness is reversibly dependent on temperature. The film thickness, corresponding to the Gibbsian surface excess of the solutes/adsorbates, decreases with decreasing temperature in

* Corresponding author. Tel.: +1 864 656 5961; fax: +1 864 656 1453.
E-mail address: jianluo@clemson.edu (J. Luo).

the subeutectic regime ($T_{\text{eutectic}} = 740\text{ °C}$ for ZnO–Bi₂O₃) until the films ultimately vanish [15]. With increasing temperature, these nanometer-thick SAFs persist into the solid–liquid two-phase regime, in equilibrium with non-wetting liquid drops [15]. This unique wetting configuration is analogous to the frustrated-complete or pseudo-partial wetting [24,25] that was proposed and confirmed for molecular substances [26].

This study further explores the unique wetting behavior in the presence of nanoscale SAFs using several experimental techniques and contributes to general high-temperature wetting and prewetting/adsorption theories. First, Bi₂O₃-enriched SAFs were found to form preferentially on {11 $\bar{2}$ 0} ZnO surfaces, while {1 $\bar{1}$ 00} facets are devoid of films (Fig. 1) [15]. The anisotropic formation of SAFs for Bi₂O₃ on ZnO provides a unique experimental opportunity to critically examine anisotropic wetting behavior with and without the presence of nanoscale SAFs. In a broader context, quantitative measurements of temperature-dependent anisotropic wetting can provide critical information about surface transitions; if anisotropic surface adsorption or structural transitions occur, comparison of wetting behavior on surfaces of different orientation at constant chemical potential can be particularly informative. To date, the only information in this regard is interesting qualitative observations made for Ge–Pb liquid on Pb in the presence of anisotropic premelting [27,28].

Second, analogous wetting and prewetting behavior is expected at free surfaces and grain boundaries. Similar force-balance and diffuse-interface models have been proposed for SAFs and IGFs [16,18,19,29]. Hot-stage in situ experiments can probe the SAF formation mechanism as well as provide insight into analogous IGF stability, where in situ experiments are more difficult to conduct.

Third, if wetting in the presence of SAFs (or IGFs) follows a generalized Cahn model, a transition to complete wetting is generally expected at a higher temperature, at which an adsorbed surficial film becomes arbitrarily thick ($h \rightarrow \infty$) and the Young contact angle vanishes ($\theta_Y = 0$) [15,16,18,20]. This is due to an entropic interaction that thickens SAFs (or IGFs) with increasing temperature

[30]. In contrast, other analyses [31] have concluded that complete wetting cannot occur in the presence of a long-range, attractive dispersion force. The apparent occurrence of complete grain boundary wetting in Bi₂O₃-doped ZnO [32,33], where stabilization of equilibrium-thickness IGFs was observed at lower temperatures supports the Cahn model [34,35]. This study further probes this controversial issue with in situ experiments for Bi₂O₃ on ZnO where the dispersion force is attractive and significant. Furthermore, the phenomena of temperature-dependent dissolution wetting, formation of faceted ridges and associated pinning effects, and anisotropic receding kinetics are carefully analyzed.

2. Experimental procedure

Bi₂O₃–ZnO beads of desired compositions were made by melting a mixture of high-purity ZnO (99.99%, Alfa Aesar) and Bi₂O₃ (99.999%, Alfa Aesar) powders. Beads of <0.1 mg were selected and used in the wetting experiments to reduce gravitational effects. High-purity (99.99%) epitaxially polished (i.e. epitaxy ready) ZnO single crystals of {11 $\bar{2}$ 0} and {1 $\bar{1}$ 00} orientations were purchased from Princeton Scientific Corporation (Princeton, NJ) and MTI Corporation (Richmond, CA). The surface roughness of the as-received crystals is about 1 nm. Crystals were ultrasonically cleaned in deionized water and acetone, and dried in air.

Bi₂O₃–ZnO beads were placed on the top of cleaned ZnO substrates, and the assemblies were used for in situ hot-stage optical microscopy measurements. Side-view experiments were conducted using a tube furnace equipped with a long-focal-length microscope and digital camera (custom made by Thoughtventions Unlimited LLC, Glastonbury, CT) to measure macroscopic contact angle as a function of temperature and other controlled parameters. Contact angles were obtained by either drawing tangent lines to experimental images or fitting of the height-to-base ratios of the sessile drops assuming hemispherical cap morphology. The latter method resulted in better repeatability ($\sim\pm 1^\circ$) between measurements. The accuracy of the side-view experiments decreases as the temperature increases

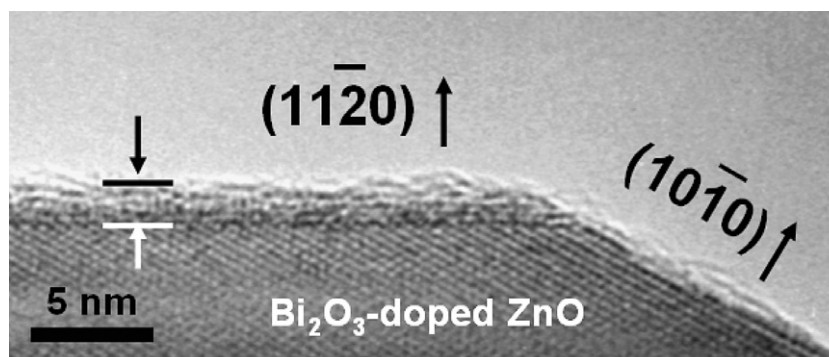


Fig. 1. HRTEM image of anisotropic formation of nanometer-thick surficial amorphous film (SAF) in Bi₂O₃-doped ZnO. The image is adapted from Ref. [13].

since the contact angle becomes small and specimen glowing increases, obscuring the image.

As complementary experiments, in situ top-view optical microscopy experiments were conducted using a Linkam hot-stage cell (Linkam Scientific Instruments, Surrey, UK) under a Leica optical microscope, where the drop radii were measured. Here the normalized radii (R/R_{\max} , where R and R_{\max} are the instantaneous and maximum radius, respectively) were recorded.

Helium (He) gas flowed through the tube furnace or the hot cell at a constant rate during the measurement. Side-view experiments were also conducted in air, and the measured results were found to be identical to those conducted in flowing He. The measurement errors for top-view experiments were estimated to be $\sim\pm 3.5\%$ from the uncertainties in determining the drop edge locations.

In most of the wetting experiments, beads containing 3 wt.% ZnO (i.e. the eutectic composition) were used, and the heating rate was kept at $10\text{ }^{\circ}\text{C min}^{-1}$. To examine the effect of temperature-dependent liquidus composition, beads containing 6 and 10 wt.% ZnO were also tested. Heating rates of 50 and $100\text{ }^{\circ}\text{C min}^{-1}$ were also examined.

Isothermal drop receding kinetics were studied by holding the Linkam hot-stage cell at a constant temperature ($1050\text{ }^{\circ}\text{C}$) under a constant He gas flow rate so that the liquid drop shrinks as Bi_2O_3 evaporates. In these experiments, a high heating rate of $100\text{ }^{\circ}\text{C min}^{-1}$ was used to minimize the effect of evaporation before reaching the testing temperature. To exclude artifacts due to ZnO precipitation, pure Bi_2O_3 beads were used in these experiments.

A Hitachi S4800 field-emission scanning electron microscope equipped with an energy-dispersive X-ray spectroscopy detector was used to characterize the wetting configuration and morphology ex situ on solidified drops. Specimens were coated with gold/platinum for characterization by scanning electron microscopy (SEM).

3. Results

3.1. Anisotropy of wetting

A typical side-view in situ optical micrograph of a liquid drop on the ZnO single-crystal surface of $\{1\bar{1}\bar{2}0\}$ orientation is shown in Fig. 2. Fig. 3a shows that measured contact angle vs. temperature for a $\text{Bi}_2\text{O}_3 + 3\text{ wt.}\%$ ZnO (eutectic) liquid drop on a ZnO $\{1\bar{1}\bar{2}0\}$ surface, where nanometer-thick SAFs are known to form (Fig. 1) [14]. On this surface, the contact angle decreases monotonically

with increasing temperature between ~ 750 and $\sim 860\text{ }^{\circ}\text{C}$, but becomes a constant value above $\sim 860\text{ }^{\circ}\text{C}$. The mean contact angle for data measured between 900 and $1000\text{ }^{\circ}\text{C}$ is 6.0° . Fig. 3a also includes contact angles measured using a larger particle (9.4 mg) vs. the standard $<0.1\text{ mg}$ particles, with air flowing instead of He, and direct measurements from images as opposed to fitting the sessile shapes; the results are all identical within the range of experimental errors. This shows that gravity, gas atmosphere and measurement method have no significant impact on the measured contact angles. The mean (solid line) and standard deviation (error bars) for several measurements made on $\{1\bar{1}\bar{2}0\}$ surfaces are also shown in Fig. 3a. Consistently, the radius of a liquid drop measured in the top-view experiments increases monotonically with increasing temperature until it levels off above $\sim 860\text{ }^{\circ}\text{C}$ (Figs. 3b and 4).

In contrast, the measured contact angle of a Bi_2O_3 -rich drop is virtually constant on the ZnO $\{1\bar{1}00\}$ surface (Fig. 3a), where nanoscale SAFs do not form (Fig. 1) [14]. The average measured contact angle on the $\{1\bar{1}00\}$ surface is about 14.6° . Consistently, the radius of a liquid drop on the ZnO $\{1\bar{1}00\}$ surface measured in a top-view experiment does not vary with temperature (Fig. 3b).

3.2. Effects of ramp rate, drop composition and hysteresis

The influence of heating rate was studied in top-view measurements, where 3 wt.% ZnO (eutectic) drops are heated at 10, 50 and $100\text{ }^{\circ}\text{C min}^{-1}$, respectively. The measured R/R_{\max} vs. temperature is virtually identical (Fig. 4a). Thus, any kinetic effects appear to be insignificant in these measurements.

While the solubility of Bi_2O_3 in ZnO crystal is minimal ($<0.06\text{ mol.}\%$ [36]), the solubility of ZnO in Bi_2O_3 liquid is more significant and temperature dependent [37]. The eutectic bulk liquid contains $\sim 3\text{ wt.}\%$ ($\sim 5\text{ vol.}\%$) ZnO at $740\text{ }^{\circ}\text{C}$; the equilibrium ZnO concentration at the liquidus increases to $\sim 6\text{ wt.}\%$ ($\sim 10\text{ vol.}\%$) at $900\text{ }^{\circ}\text{C}$ and $\sim 9\text{ wt.}\%$ ($\sim 15\text{ vol.}\%$) at $1050\text{ }^{\circ}\text{C}$, respectively [37]. Thus, some ZnO from the substrate will be dissolved in the liquid during continuous heating, creating a concave pit on the substrate. To examine this effect, three starting ZnO compositions (3, 6 and 10 wt.%, respectively) are used in top-view measurements. When the ZnO content in the starting bead is higher than that in the eutectic liquid, the liquid drop formed at lower temperatures contains some floating ZnO particles, resulting in an experimental artifact of

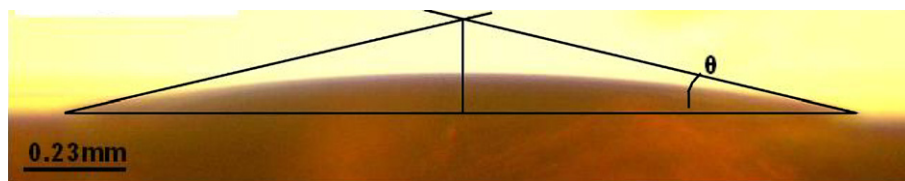


Fig. 2. Representative in situ hot-stage optical micrograph of a Bi_2O_3 -enriched drop on a ZnO $\{1\bar{1}\bar{2}0\}$ single crystal (side view).

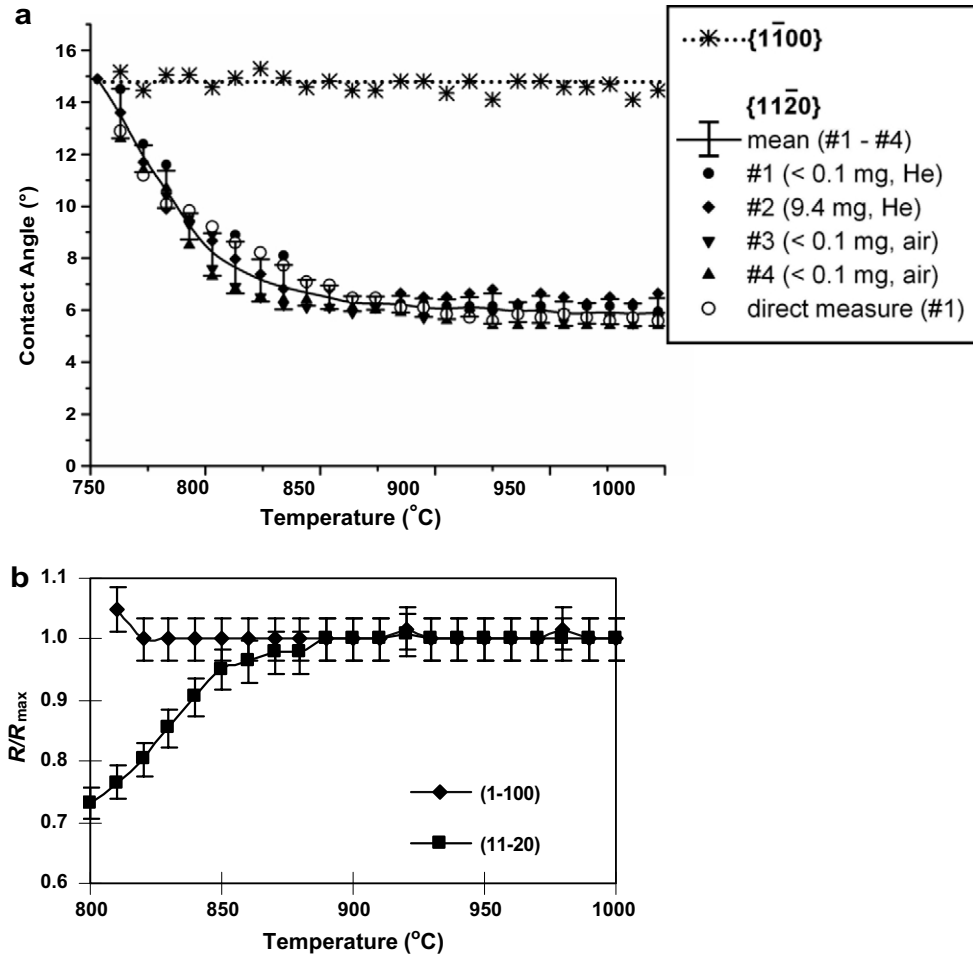


Fig. 3. (a) Contact angle vs. temperature measured in side-view experiments and (b) normalized radius vs. temperature measured in top-view experiments. The specimens are eutectic (3 wt.% ZnO) liquid drops on ZnO $\{11\bar{2}0\}$ and $\{1\bar{1}00\}$ surfaces, heated at a rate of $10\text{ }^\circ\text{C min}^{-1}$. The error bars for the individual measurements ($\sim \pm 1^\circ$ in repeatability) are not shown in (a) for figure clarity; the means and standard deviations of multiple measurements for drops on $\{11\bar{2}0\}$ surfaces using different conditions are shown.

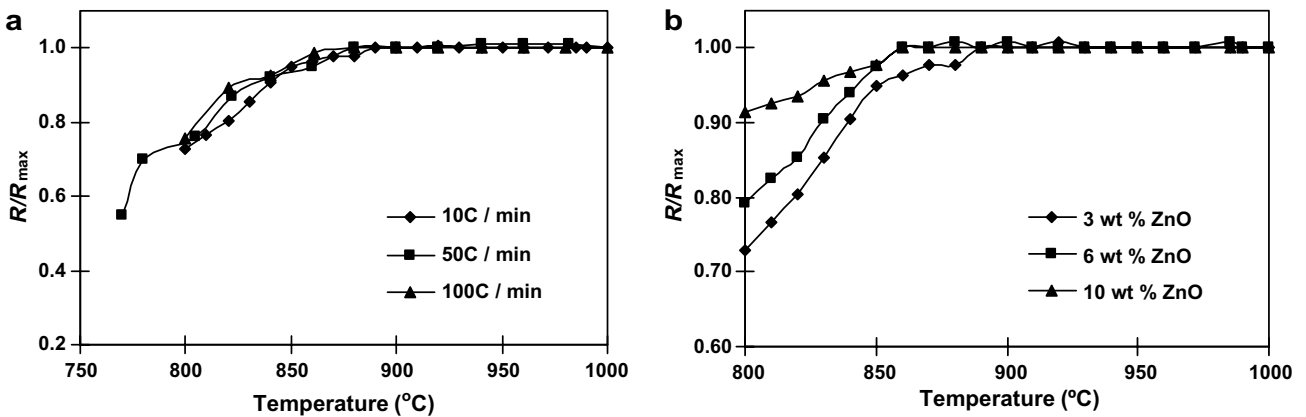


Fig. 4. Normalized radius vs. temperature for experiments using different (a) heating rates and (b) starting drop compositions. Error bars ($\pm 3.5\%$) are not shown for figure clarity.

apparently greater R/R_{max} , as shown in Fig. 4b. Nonetheless, Fig. 4b illustrates that the contact angle (represented by R/R_{max}) levels at $\sim 860^\circ\text{C}$ irrespective of the starting composition.

To probe the hysteresis effect, specimens were heated to temperatures of ~ 850 , ~ 900 and 1037°C , respectively, and then cooled with the furnace shut down. The receding contact angles vs. temperatures measured during cooling are

shown in Fig. 5, in which the envelope of advancing contact angles measured during heating is re-plotted for comparison. A significant hysteresis effect is evident. Notably, most drops do not recede significantly until $\sim 750^\circ\text{C}$ during continuous cooling at $\sim 7\text{--}10^\circ\text{C min}^{-1}$, presumably due to a strong ridge pinning effect at the triple lines (see Sections 3.3 and 4.2 for elaboration). When a drop does recede, it does not always maintain a circular symmetry (Figs. 6a and 7c). If non-circular receding occurs, side-view experiments can no longer accurately measure contact angles.

3.3. Faceted ridges

SEM images of Bi_2O_3 -rich drops on ZnO $\{11\bar{2}0\}$ surfaces cooled from 950 and 1050°C are shown in Fig. 6, where the solidified drops are removed in Fig. 6a, b and d. The existence of wetting ridges at the triple lines [38–40] is evident in Fig. 6b. Figs. 6c and d are images of the ridges viewed at expanded views, showing the formation of faceted terraces. Several secondary ridges are also seen in Fig. 6a, indicating that the drop does not recede continuously; nor does it retain a circular symmetry during recession. In Fig. 6c, the solidified drop, which has receded during cooling, can be seen.

3.4. Anisotropy in isothermal drop receding kinetics

Since the contact angle hysteresis is significant (presumably due to ridge pinning) (Fig. 5), it is important to clarify whether complete wetting is inhibited by ridge pinning. To probe any kinetic effect that hinders the drop advancement

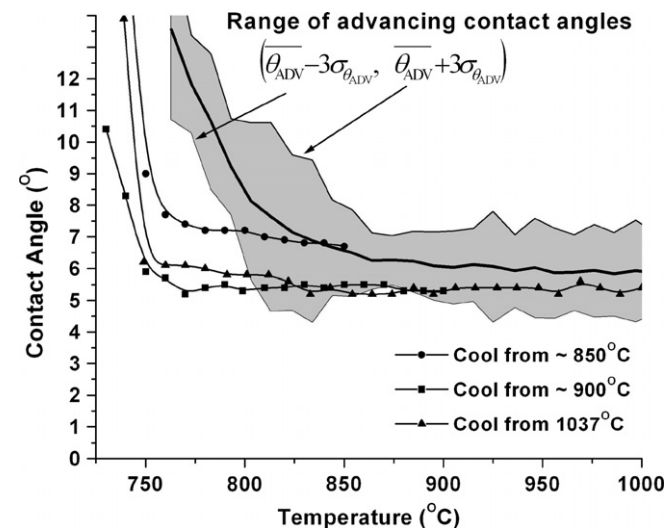


Fig. 5. Contact angle vs. temperature for selected specimens during cooling. The specimens are $\text{Bi}_2\text{O}_3 + 3 \text{ wt.}\% \text{ ZnO}$ drops on $\{11\bar{2}0\}$ surfaces, and the cooling rates are $7\text{--}10^\circ\text{C min}^{-1}$. The envelope of advancing contact angles measured during heating (means ± 3 standard deviations) is also re-plotted as a reference. The error bars for the individual measurements ($\sim \pm 1^\circ$ for repeatability) are not shown for figure clarity.

and to further estimate a receding contact angle as a lower bound of the Young contact angle (Section 4.3), isothermal drop receding experiments were conducted at 1050°C by allowing Bi_2O_3 to evaporate continuously. (See Section 2 for experimental settings and Section 4.3 for a proposed kinetic model.) Fig. 7a is an in situ optical micrograph of a drop on a $\{1\bar{1}00\}$ surface after 8 min of isothermal evaporation. On this surface orientation, a drop recedes uniformly and maintains a circular symmetry (until significant ZnO precipitation occurs). On the other hand, a drop on the $\{11\bar{2}0\}$ surface recedes non-uniformly (no longer circular) and by discrete jumps (due to ridge pinning). This is evident in Fig. 7c, which shows a drop on a ZnO $\{11\bar{2}0\}$ surface after 10.5 min of isothermal evaporation. Discrete jumps during drop receding were recorded by in situ video images and were evident by the secondary ridges in the SEM images (Fig. 6a) and optical micrographs (Fig. 7c).

Fig. 7b shows the measured $R(t)/R_{\text{max}}$ vs. time during isothermal drop evaporation and receding on the $\{1\bar{1}00\}$ surface. For non-circular drop receding on the $\{11\bar{2}0\}$ surface, $\sqrt{A(t)/A_{\text{max}}}$ vs. time was recorded and is shown in Fig. 7d, where $A(t)$ and A_{max} are the instantaneous and maximum projected areas of the drop on the surface, respectively; the function $\sqrt{A(t)/A_{\text{max}}}$ is equal to $R(t)/R_{\text{max}}$ for a circular drop and represents a “normalized equivalent radius” for noncircular drops. The observed $\sqrt{A(t)/A_{\text{max}}}$ vs. time is not continuous (Fig. 7d) due to the occurrence of discrete receding jumps on the $\{11\bar{2}0\}$ surface.

The drop on the ZnO $\{1\bar{1}00\}$ surface recedes almost instantaneously after reaching the holding temperature (Fig. 7b). On the other hand, receding occurs on the $\{11\bar{2}0\}$ surface after ~ 6 min of isothermal evaporation (Fig. 7d). Presumably, evaporation occurs continuously, but the drop is pinned by the ridge at the triple line before receding. The reduction in the liquid drop volume is achieved by adjusting the macroscopic contact angle from θ_{ADV} (the advancing contact angle) to θ_{REC} (the receding contact angle) before the drop starts to recede. The observed $\sqrt{A(t)/A_0}$ or $R(t)/R_0$ decreases almost linearly with time once the drop receding starts (Fig. 7b and d). With several approximations, a kinetic model is proposed for this unique two-step drop receding process in Section 4.3 to estimate the macroscopic receding contact angle ($\theta_{\text{ADV}} > \theta_Y > \theta_{\text{REC}} > 0$).

4. Discussion

4.1. Macroscopic wetting configuration

Since the solubility of ZnO in Bi_2O_3 -rich liquid increases with increasing temperature, the present experiments represent a case of temperature-dependent dissolution wetting. Fig. 8a schematically illustrates a macroscopic wetting configuration, in which interfacial energies are assumed to be isotropic for simplicity. It is reasonable to assume that ZnO dissolution is rapid, so local chemical equilibrium is

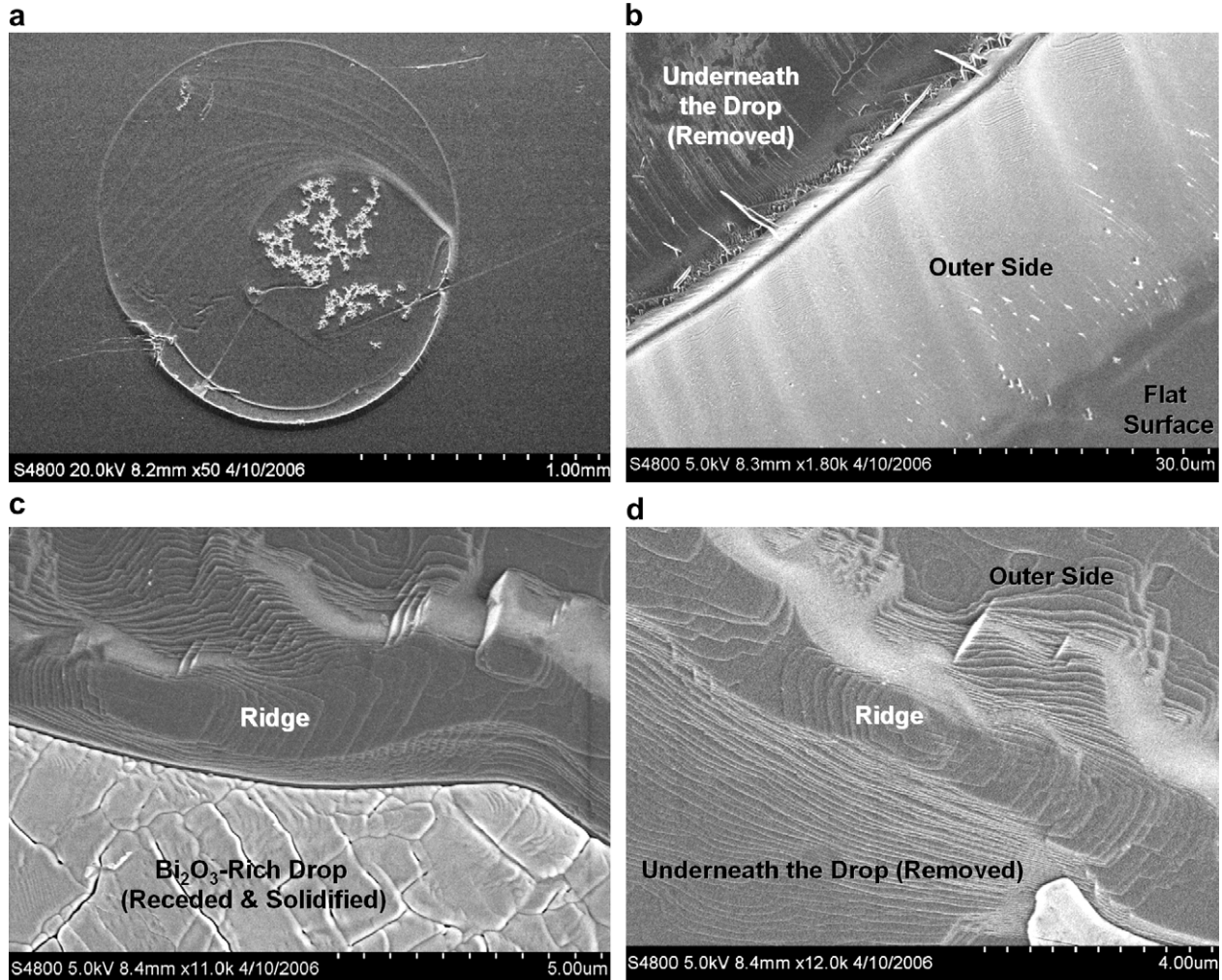


Fig. 6. Representative SEM images of the faceted ridges at the triple lines. Solidified drops have been removed in (a), (b) and (d).

achieved while long-range diffusion in the solid substrate is insignificant in the experimental time scale. Thus, the substrate surface remains flat except for the region near the triple line. The liquid drop consists of two parts, V_0 and V' , i.e. the volumes of the liquid above and below the horizontal plane, respectively. With increasing temperature, a liquid drop will consume more ZnO from the substrate. To the first order of approximation, the volume change upon the dissolution and the evaporation of Bi₂O₃ are neglected. Hence, V_0 is a constant and V' increases with increasing temperature.

To estimate measurement errors in the Young contact angles (this section), and to further analyze the drop receding kinetics (Section 4.3), basic geometrical relations for the wetting configurations shown in Fig. 8 are given as follows. The volume of a sessile drop is

$$V_0 = \frac{\pi R^3}{3} \cdot \frac{(2 - 3 \cos \theta + \cos^3 \theta)}{\sin^3 \theta} = \frac{\pi}{4} R^3 \theta + o(\theta) \quad (\theta \ll 1) \quad (1)$$

where θ is the apparent contact angle and R is the projected radius from the top view (Fig. 7). A similar relationship can

be used to compute (or estimate, in the case of anisotropic interfacial energies) the liquid volume below the horizontal line:

$$V' = \frac{\pi}{4} R^3 \theta' + o(\theta') \quad (\theta' \ll 1) \quad (2)$$

Combining Eqs. (1) and (2) yields

$$\frac{\theta'}{\theta} \approx \frac{V'}{V_0} \quad (3)$$

Then, the relationship between the real Young contact angle θ_Y (without dissolution) and the measured apparent contact angle θ is derived as follows:

$$\theta < \theta_Y < (\theta + \theta') \approx (1 + V'/V_0)\theta \quad (4)$$

Thus, the error in measuring the Young contact angle is estimated as

$$0 < \frac{\theta_Y - \theta}{\theta_Y} < \frac{V'}{V_0} \quad (5)$$

For Bi₂O₃ drops on ZnO {11 $\bar{2}$ 0} surfaces, however, the interfacial energies are anisotropic. In particular, the bottom of the liquid drop should be flat because of the low

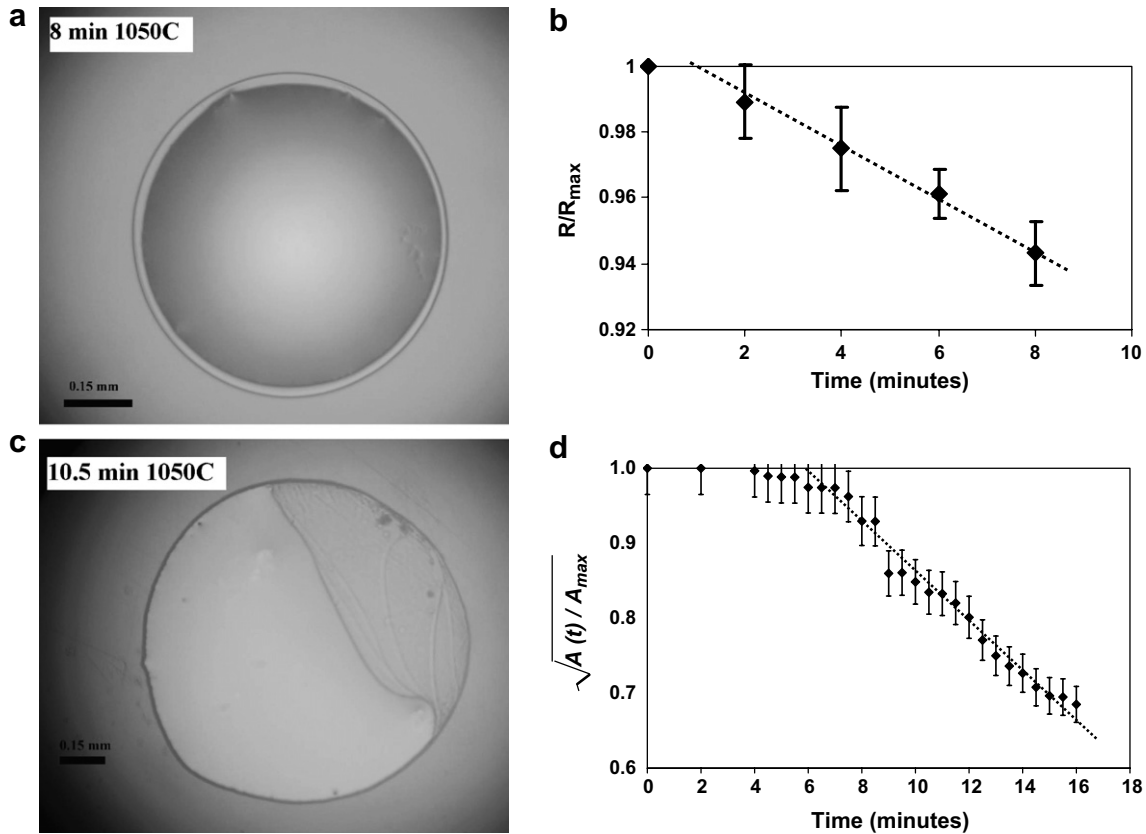


Fig. 7. (a) A representative in situ optical micrograph from an isothermal drop receding experiment conducted on a ZnO $\{1\bar{1}00\}$ surface and (b) the corresponding $R(t)/R_{\max}$ vs. time. Error bars in (b) represent the standard deviations of measurements of diameters along four directions. (c) A representative in situ optical micrograph for an isothermal drop receding experiment conducted on a ZnO $\{11\bar{2}0\}$ surface and (d) the corresponding $\sqrt{A(t)/A_{\max}}$ vs. time.

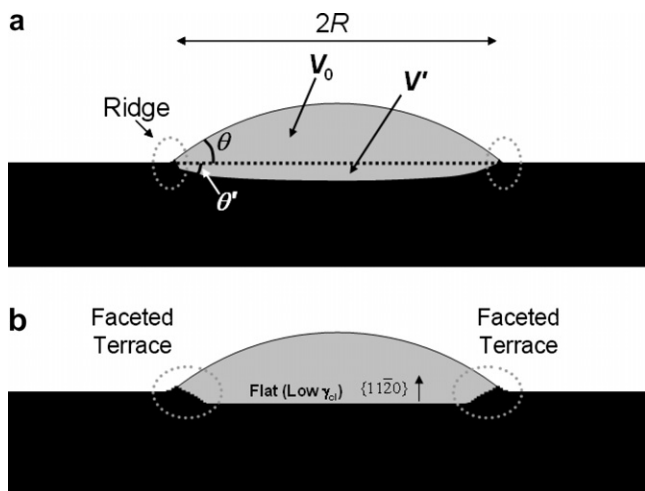


Fig. 8. (a) Macroscopic wetting configuration assuming isotropic interfacial energies. V_0 is roughly a constant; V'/V_0 and θ'/θ are small. (b) For Bi₂O₃ drop on the ZnO $\{11\bar{2}0\}$ surface, the bottom of the liquid drop should be flat and there are faceted terraces near the triple line. See text for elaboration.

interfacial energy between the ZnO $\{11\bar{2}0\}$ surface and the Bi₂O₃ liquid [14], and there are faceted terraces near the triple line (Figs. 6 and 8b). Nonetheless, Eq. (5) can be used to obtain a rough estimate. The Bi₂O₃-rich liquid in equilib-

rium with ZnO contains 5 vol.% ZnO at 740 °C ($=T_{\text{eutectic}}$), 9 vol.% ZnO at 900 °C and 15 vol.% ZnO at 1050 °C, respectively [37]. For the experiments using eutectic beads, V'/V_0 is calculated to be 0.044 at 900 °C and 0.118 at 1050 °C, respectively. Since experiments were conducted up to 1050 °C but the contact angle levels when the temperature is greater than ~ 860 °C, the measured errors in the Young contact angles are $<12\%$ overall and $<5\%$ for the significant part of T -dependent contact angle measurements. These errors are, in general, less than the measurement errors; therefore they are insignificant.

Additionally, the surface area of a liquid drop is

$$A = 2\pi R^2 \cdot \frac{1 - \cos \theta}{\sin^2 \theta} \approx \pi R^2 + o(\theta) \quad (\theta \ll 1) \quad (6)$$

Eqs. (1) and (6) are used in assessing the receding kinetics of the drop in Section 4.3.

4.2. Faceted ridges and hysteresis

The formation of ridges at triple lines as a result of the unbalanced vertical interfacial force component was previously studied for metal liquid drops on ceramic substrates [38–40], where isotropic interfacial energies were assumed and observed. The present case is more intriguing as the

ridges are faceted terraces (Fig. 6). Anisotropic ridge formation was also previously observed for another system – Cu on Al₂O₃ – which exhibits a different morphology [41].

Ridging effect can hinder the advancement of a liquid drop [38–41]. If complete wetting occurs and interfacial energies are isotropic, ridges cannot inhibit the spreading, and a liquid drop can flow over ridges of any shape. However, ridges with partial-wetting facets can block the spreading. This possibility motivated the isothermal drop receding experiments (Section 3.4), which revealed unique two-stage receding kinetics, leading to the conclusion that complete wetting does not occur (Section 4.3).

Even if the inhibition of complete wetting is not (wholly) due to ridge pinning, the existence of faceted ridges can result in significant hysteresis. The proposed triple-line configurations at equilibration and during drop advancing and receding are schematically illustrated in Fig. 9. Such hysteresis effect results in different advancing and receding contact angles ($\theta_{\text{REC}} < \theta_Y < \theta_{\text{ADV}}$). Indeed, strong pinning effects on cooling (Fig. 5) and during isothermal drop receding (Fig. 7d, represented by the incubation time) were observed on $\{11\bar{2}0\}$ surfaces.

4.3. Isothermal drop receding kinetics

Assuming the evaporation rate is proportional to the surface area during isothermal drop receding, the following kinetic equation can be proposed:

$$\frac{dV}{dt} = -K \cdot A \quad (7)$$

where K is a kinetic constant and a function of the temperature, the gas flow rate and the vapor pressure in the chamber (which, in turn, depends on the chamber geometry).

The isothermal evaporation process can be divided into two stages. In the first stage, the reduction in liquid volume due to evaporation leads to the change of the contact angle from θ_{ADV} to θ_{REC} (without receding). The existence of this stage implies an incubation time period ($\Delta t_{\text{incubation}}$) before the drop starts to recede, which was observed in experiments (Fig. 7b and d). The incubation time period is significant for the drop on the $\{11\bar{2}0\}$ surface (Fig. 7d), implying a large ($\theta_{\text{ADV}} - \theta_{\text{REC}}$). If Eqs. (1) and (6) are substituted into Eq. (7) and it is assumed that the contact angle is small for the isothermal drop receding on the

$\{11\bar{2}0\}$ surface at 1050 °C, the following relation can be derived:

$$d\theta = -\frac{4K}{R} \cdot dt \quad (8)$$

Integrating the above equation produces:

$$\theta_{\text{ADV}} - \theta_{\text{REC}} = \frac{4K}{R_{\text{max}}} \cdot \Delta t_{\text{incubation}} \quad (9)$$

for small θ . A precise relation can also be deduced for large θ .

In the second stage, the drop retracts with a constant contact angle (θ_{REC}). If a drop maintains a circular symmetry, combining Eqs. (1), (6) and (7) produces:

$$\frac{dR}{dt} = -K \cdot \frac{2(1 - \cos \theta_{\text{REC}}) \sin \theta_{\text{REC}}}{(2 - 3 \cos \theta_{\text{REC}} + \cos^3 \theta_{\text{REC}})} \quad (10)$$

For small θ , the above kinetic equation is simplified to

$$\frac{dR}{dt} \approx -\frac{4K}{3\theta_{\text{REC}}} \quad (11)$$

Indeed, a linear kinetic regime for the retraction of a drop on the $\{1\bar{1}00\}$ surface was observed (Fig. 7b), showing the validity of the proposed kinetic model. A linear regression for the data shown in Fig. 7b is conducted. The retraction rate in the linear regime was found to be $d(R/R_{\text{max}})/dt = -0.0076/\text{min}$ or $dR/dt = -2.67 \mu\text{m}/\text{min}$, with an incubation time $\Delta t_{\text{incubation}} = 0.68 \text{ min}$. The correlation factor (r^2) is calculated to be 0.9959.

To estimate the receding contact angle, combining Eqs. (9) and (11) gives:

$$\theta_{\text{ADV}} - \theta_{\text{REC}} = -\frac{d(R/R_{\text{max}})}{dt} \cdot \Delta t_{\text{incubation}} \cdot 3\theta_{\text{REC}} \quad (12a)$$

Since $\Delta t_{\text{linear retraction}} \equiv -1/[d(R/R_{\text{max}})/dt]$ is the projected total time period for the stage-two drop receding, Eq. (12a) can be rewritten (to show a clear physical explanation) as

$$\frac{\theta_{\text{ADV}} - \theta_{\text{REC}}}{\theta_{\text{REC}}} = \frac{\Delta t_{\text{incubation}}}{\Delta t_{\text{linear retraction}}/3} \quad (12b)$$

On the $\{11\bar{2}0\}$ surface, the drop no longer maintains a circular symmetry during recession. Nonetheless, to the first order approximation, Eqs. (11) and (12) can be modified by replacing R with an equivalent radius, $\bar{R} \equiv \sqrt{A/\pi}$ ($\bar{R}/R_{\text{max}} \equiv \sqrt{A/A_{\text{max}}}$), as

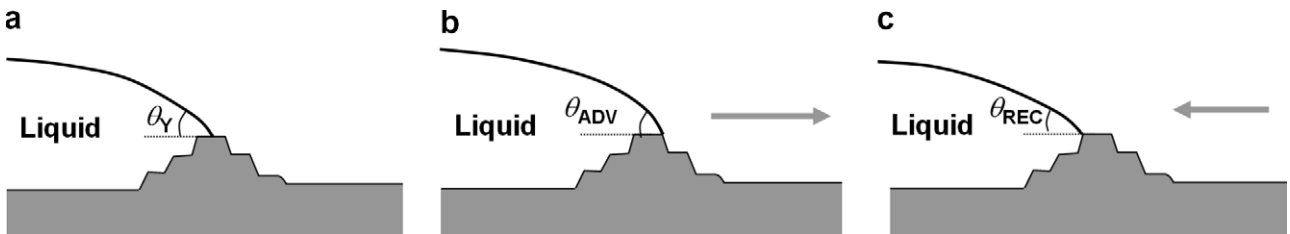


Fig. 9. (a) Schematic illustration of the faceted ridges at the triple line. Proposed configurations during the (b) advancing and (c) receding of a liquid drop. $\theta_{\text{REC}} < \theta_Y < \theta_{\text{ADV}}$.

$$\frac{d\bar{R}}{dt} = \frac{d\sqrt{A/A_{\max}}}{dt} \cdot R_{\max} \approx -\frac{4K}{3\theta_{\text{REC}}} \quad (13)$$

and

$$\theta_{\text{ADV}} - \theta_{\text{REC}} = -\frac{d\left(\sqrt{A/A_{\max}}\right)}{dt} \cdot \Delta t_{\text{incubation}} \cdot 3\theta_{\text{REC}} \quad (\theta \ll 1) \quad (14)$$

The above approximation is valid based on the assumption that $V/A \approx \bar{R}\theta_{\text{REC}}/4$, and its validity is supported by the linear relation shown in Fig. 7d.

A linear receding regime (with steps due to the ridge pinning) after a rather long incubation time is shown in Fig. 7d for a drop on the $\{11\bar{2}0\}$ surface. A linear regression of the data shown in Fig. 7d is conducted (resulting in a correlation factor: $r^2 = 0.98$). The retraction rate in the linear regime is found to be $d\sqrt{A/A_{\max}}/dt = -0.0322/\text{min}$ or $d\bar{R}/dt = -17.5 \mu\text{m}/\text{min}$. The incubation time ($\Delta t_{\text{incubation}}$) is found to be 5.6 min. Thus, the receding contact angle on the $\{11\bar{2}0\}$ surface is estimated from Eq. (14) to be

$$\theta_{\text{REC}}^{\{11\bar{2}0\}} = \frac{\theta_{\text{ADV}}^{\{11\bar{2}0\}}}{1 - 3\Delta t_{\text{incubation}} \cdot \frac{d\left(\sqrt{A/A_{\max}}\right)}{dt}} = 3.86^\circ \approx 4^\circ \quad (15a)$$

Similarly, the receding contact angle on the $\{1\bar{1}00\}$ surface is estimated to be $\theta_{\text{REC}}^{\{1\bar{1}00\}} = 14.4^\circ$ (which is only slightly lower than $\theta_{\text{ADV}}^{\{1\bar{1}00\}} = 14.6^\circ$).

In a second approach, $\theta_{\text{REC}}^{\{11\bar{2}0\}}$ is alternatively estimated with the assumption that the kinetic constant K in Eq. (7) is identical for experiments that were conducted under the same conditions. Then, K is calculated to be $0.5 \mu\text{m min}^{-1}$ using Eq. (10) and the experimental data obtained for the stage-two drop receding on the $\{1\bar{1}00\}$ surface (Fig. 7b). This calculated K value should be reliable since the drop maintains a circular symmetry on the $\{1\bar{1}00\}$ surface, the contact angle is high and the exact mathematical equation (Eq. (10)) is used. Then, $\theta_{\text{REC}}^{\{11\bar{2}0\}}$ is estimated by rewriting Eq. (9):

$$\theta_{\text{REC}}^{\{11\bar{2}0\}} = \theta_{\text{ADV}}^{\{11\bar{2}0\}} - 4K \left(\frac{\Delta t_{\text{incubation}}}{R_{\max}} \right)_{\{11\bar{2}0\}} \cdot \frac{180^\circ}{\pi} = 4.8^\circ \quad (15b)$$

This result agrees well with the estimate obtained using the first approach in Eq. (15a). Since Eq. (15b) estimates $\theta_{\text{REC}}^{\{11\bar{2}0\}}$ by comparing the stage-one drop receding kinetics on the $\{11\bar{2}0\}$ surface with the stage-two kinetics on the $\{1\bar{1}00\}$ surface, errors associated with non-circular drop retraction are eliminated, and the mathematical model for approach 2 is rigorous.

In summary, analysis of isothermal receding kinetics demonstrates first that a ridge pinning effect results in observable differences in drop advancing and receding contact angles on the $\{11\bar{2}0\}$ surface. Second, complete wetting does not occur on the $\{11\bar{2}0\}$ surface at 1050°C . The estimated range of the equilibrium Young contact angle is

$$\sim 4^\circ \approx \theta_{\text{REC}}^{\{11\bar{2}0\}} < \theta_{\text{Y}}^{\{11\bar{2}0\}} < \theta_{\text{ADV}}^{\{11\bar{2}0\}} \approx 6^\circ \quad (16)$$

Third, the wetting configurations and drop receding (or advancing) kinetics on the $\{11\bar{2}0\}$ surface differ significantly from those on the $\{1\bar{1}00\}$ surface.

4.4. Wetting in the presence of nanoscale SAFs

Analogous conditions of nanoscale surficial films in equilibrium with a partial-wetting drop have been observed in organic or aqueous systems and are termed “frustrated-complete wetting” [26], although, to our knowledge, this is the first such study of a high-temperature inorganic system. A similar condition of a partial-wetting drop surrounded by a thin pure liquid film with thickness limited by London dispersion forces has been termed “pseudo-partial wetting” [24] or “autophobic wetting” [42]. Various thermodynamic models have been proposed for wetting and adsorption transitions, and these models generally follow the Cahn critical point wetting model [20]. Relevant wetting phenomena have been reviewed by de Gennes [25], Dietrich [30], and Bonn and Ross [43].

A schematic illustration of the wetting configuration on ZnO $\{11\bar{2}0\}$ surface in the presence of SAFs is shown in Fig. 10a. In a phenomenological thermodynamic model, the excess free energy of a surficial liquid film with thickness h is given by

$$G^x(h) = (\gamma_{\text{cl}} + \gamma_{\text{lv}}) + \sigma_{\text{interfacial}}(h) \quad (17)$$

where $(\gamma_{\text{cl}} + \gamma_{\text{lv}})$ represents the sum of crystal–liquid and liquid–vapor interfacial energies. When the film is thin, an extra interfacial free energy term $\sigma_{\text{interfacial}}(h)$ (i.e. $\omega(l)$ in Dietrich’s review [30], $P(\zeta)$ in de Gennes review [25] or $E_{\text{int}}(h)$ in a recent critical review of quasi-liquid interfacial films [18]) arises, representing the total contribution of all interfacial forces. (An additional volumetric thermodynamic term $\Delta\mu \cdot \rho \cdot h$ should be added for quasi-liquid films formed at subsolidus conditions.) The term $\sigma_{\text{interfacial}}(h)$ is equal to an integral of the “disjoining pressure” (as defined by Deryaguin) from h to ∞ [25]. By definition, $\sigma_{\text{interfacial}}(h)$ vanishes as $h \rightarrow \infty$. For SAFs in oxides, $\sigma_{\text{interfacial}}(h)$ can be expressed as [14–16,18]:

$$\sigma_{\text{interfacial}}(h) = \frac{A_{123}}{12\pi h^2} + \sigma_{\text{short-range}}(h) + \sigma_{\text{elec}}(h) + \dots \quad (18)$$

The first term is a long-range dispersion interaction where A_{123} is the Hamaker constant (coefficient) for the system “substrate (1)/film (2)/air (3)”. The term $\sigma_{\text{short-range}}(h)$ is a (coupled) short-range interaction of structural and chemical origins, and $\sigma_{\text{elec}}(h)$ is an electrostatic interaction. For consistency, all the interfacial free energy terms are defined so that they vanish as $h \rightarrow +\infty$. All σ terms in Eq. (18) are free energies (although the symbol E was used for these terms in several earlier articles [14,16,18]).

An “equilibrium” thickness represents a balance among the attractive and repulsive interfacial pressures/forces. The equilibrium thickness corresponds to a global or local minimum in excess film free energy vs. thickness, which is defined by

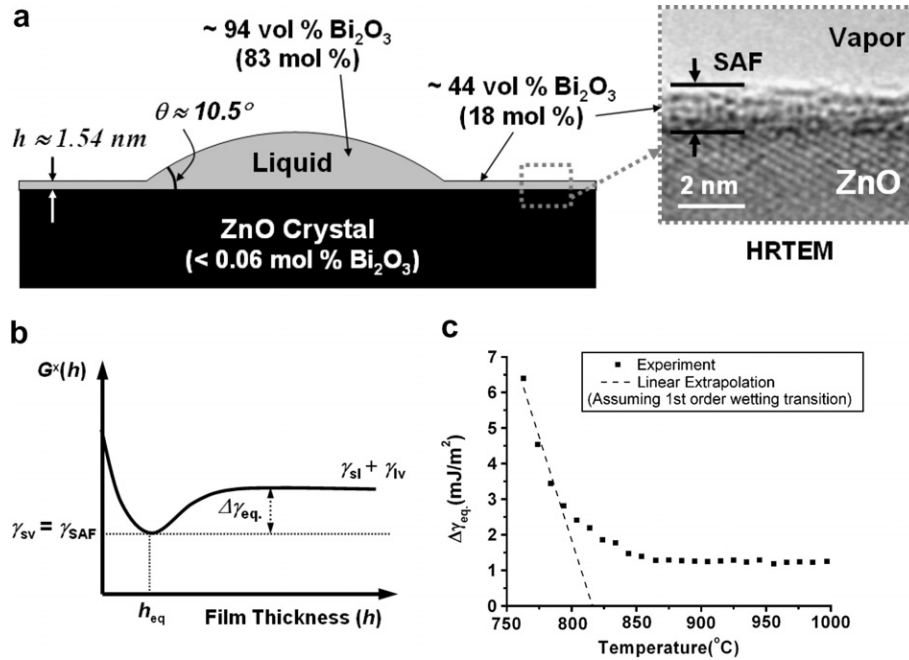


Fig. 10. (a) Schematic illustration of the equilibrium surface wetting and adsorption configuration for a Bi₂O₃-rich drop on the ZnO {11 $\bar{2}$ 0} surface at 780 °C. Film thickness and composition data are taken from Ref. [14]. (b) Schematic representation of excess surface free energy vs. film thickness in a case where a nanometer-thick SAF is stable. (c) $\Delta\gamma_{eq}$. vs. temperature calculated from the measured mean contact angles shown in Fig. 3a. Extrapolation from the data between 750 and 800 °C would project a first-order complete wetting transition at 818 °C (dashed line). If the wetting transition is critical, the projected complete wetting temperature (without the attractive dispersion force) depends on the (unknown) critical exponent. In the present case, the occurrence of complete wetting is inhibited and the observed “residual” $\Delta\gamma_{eq}$. of ~ 1 mJ m⁻² can be quantitatively explained from the magnitude of a long-range, attractive London dispersion force.

$$\left. \frac{d[G^x(h)]}{dh} \right|_{h=h_{eq}} = 0 \quad (19)$$

If an equilibrium-thickness SAF corresponds to a global minimum in excess free energy, then

$$\gamma_{sv} = \gamma_{SAF} = (\gamma_{cl} + \gamma_{lv}) + \sigma_{interfacial}(h_{eq.}) \quad (20)$$

In the present condition, an SAF (instead of a dry surface) represents the thermodynamic equilibrium configuration ($\gamma_{sv} \equiv \gamma_{SAF}$). At a thermodynamic equilibrium, the contact angle is defined by the Young equation,

$$\gamma_{sv} = \gamma_{sl} + \gamma_{lv} \cdot \cos \theta_Y \quad (21)$$

Combining Eqs. (20) and (21) gives:

$$\cos \theta_Y = \frac{\gamma_{sv} - \gamma_{sl}}{\gamma_{lv}} = 1 - \frac{\Delta\gamma_{eq.}}{\gamma_{lv}} \quad (22)$$

where

$$\begin{aligned} \Delta\gamma_{eq.} &\equiv -\sigma_{interfacial}(h_{eq.}) \equiv \gamma_{sl} + \gamma_{lv} - \gamma_{SAF} \\ &\equiv \gamma_{sl} + \gamma_{lv} - \gamma_{sv} \end{aligned} \quad (23)$$

A schematic illustration of G^x vs. h and the definition of $\Delta\gamma_{eq.}$ are shown in Fig. 10b. In general, the film thickness ($h_{eq.}$) increases and the contact angle (θ_Y) decreases with increasing temperature along the liquid–vapor coexistence line.

In wetting theories [30], the thickening of a surficial film with increasing temperature is explained as a competition

between entropy and energy (or enthalpy at a constant pressure). As temperature increases, the liquid–vapor interface tends to avoid the solid–liquid interface, which hinders interfacial fluctuation. With only short-range interactions, a complete wetting transition should occur at some higher temperature (as the system approaches a critical point), where $h_{eq.} \rightarrow \infty$, $\Delta\gamma_{eq.} \rightarrow 0$ and $\theta_Y \rightarrow 0$. If the wetting transition is first order, $\Delta\gamma_{eq.} \propto (T_W - T)$, $\theta_Y \propto (T_W - T)^{1/2}$ and $h_{eq.}$ jumps discretely to infinity at the wetting temperature T_W . If a critical (high-order or continuous) wetting transition occurs, $\Delta\gamma_{eq.} \propto (T_W - T)^{2-\alpha_s}$ (where α_s is an exponent that depends on the details of molecular interactions) and $h_{eq.}$ is divergent continuously at T_W .

A monotonic decrease of contact angle with increasing temperature is evident for the drop on the {11 $\bar{2}$ 0} surface (Fig. 3) in the presence of an SAF. As a comparison, the contact angle is a constant for the drop on the {1 $\bar{1}$ 00} surface (Fig. 3) in the absence of an SAF. This suggests that high-temperature wetting in the presence of SAFs can be described by the generalized Cahn wetting theory. Since $\gamma_{lv} \approx 200$ mJ/m² for this system, $\Delta\gamma_{eq.}(T)$ can be estimated by rewriting Eq. (22) and combining it with the measured contact angles as shown in Fig. 3a:

$$\Delta\gamma_{eq.}(T) = \gamma_{lv}(1 - \cos \theta) \approx 200 \cdot (1 - \cos \theta) \text{ mJ/m}^2 \quad (24)$$

Fig. 10c shows $\Delta\gamma_{eq.}$ vs. T . The advancing contact angles are used for calculating Fig. 10c, which probably overestimates $\Delta\gamma_{eq.}(T)$ slightly. Nonetheless, Fig. 10c shows that

$\Delta\gamma_{\text{eq.}}$ decreases monotonically between 780 and ~ 860 °C, but complete wetting does not occur (presumably being inhibited by an attractive long-range dispersion interaction; see Section 4.5 for elaboration). If a first-order wetting transition took place without this inhibition, the projected complete wetting transition temperature would be ~ 818 °C from a linear extrapolation of the T -dependent regime (with a correlation factor $r^2 = 0.9923$). Alternatively, if critical wetting took place without the inhibition, the projected complete wetting transition should depend on the specific (unknown) exponent.

A related observation was made for Ga–Pb liquid drops on a Pb solid surface, in which wetting of micron-sized Pb crystals by small Ga–Pb droplets was studied by a scanning Auger microprobe [27,28]. The wettability was found to be strongly correlated to the degree of premelting of the Pb surfaces (i.e. the formation of thin quasi-liquid surficial films below the bulk melting temperature). Below the premelting temperature of Pb, liquid Ga–Pb droplets were found to reside only on the high-energy $\{210\}$ facets of Pb. At higher temperatures, where most facets of Pb premelt, Ga–Pb droplets scatter to other orientations, showing that the formation of quasi-liquid surficial films enhances the wettability. This case is somewhat different from the present study in that Ga does not tend to segregate to the Pb surface; nonetheless, the quasi-liquid premelting films must contain some Ga due to entropic effects. This qualitative observation shows that at least one binary metallic system exhibits similar wetting behavior to the present binary oxide system.

4.5. Inhibition of complete wetting by the dispersion force

The inhibition of complete wetting is perhaps not surprising since this system exhibits a long-range dispersion force of significant strength. For a Bi_2O_3 -rich eutectic liquid film on a ZnO surface, the Hamaker constant/coefficient for SAFs was calculated to be $A_{123} = +137$ zJ [14], which is significantly greater than that for IGFs in the same system ($A_{121} \approx 58$ zJ using a single-oscillator estimation based on $n_{\text{ZnO}} = 2.02$ and $n_{\text{Bi}_2\text{O}_3} = 2.63$ [44]; a lower estimated value of +4 zJ was cited in Refs. [3,45]). If the dispersion interaction is attractive and is the longest-range force, theoretically complete wetting cannot occur as previously pointed out by Lipowsky [31]. An analysis using a continuum model by de Gennes also showed that a long-range force can suppress the complete wetting transition that would otherwise occur as the system approaches its critical point [30].

If the equilibrium thickness results from a balance between the dispersion force and a dominant short-range repulsion of exponentially decaying form ($C \cdot \exp(-h/\xi)$), where ξ is a coherent length on the atomic distance), the following relation can be derived from Eq. (19):

$$\frac{C}{\xi} \cdot e^{-h_{\text{eq.}}/\xi} = \frac{A_{123}}{6\pi h_{\text{eq.}}^3} \quad (25)$$

Thus,

$$\begin{aligned} \Delta\gamma_{\text{eq.}} &\equiv -\sigma_{\text{interfacial}}(h_{\text{eq.}}) = \frac{A_{123}}{12\pi h_{\text{eq.}}^2} - C \cdot e^{-h_{\text{eq.}}/\xi} \\ &= \frac{A_{123}}{12\pi h_{\text{eq.}}^2} \cdot (1 - 2\xi/h_{\text{eq.}}) \end{aligned} \quad (26)$$

For Bi_2O_3 -rich SAFs on ZnO, the dispersion energy $A_{123}/(12\pi h_{\text{eq.}}^2)$ is calculated to be ~ 0.9 mJ for a 2-nm-thick film and ~ 0.4 mJ for a 3-nm-thick film, respectively. Assuming a typical ξ of 0.3 nm, $\Delta\gamma_{\text{eq.}}$ is estimated to be 0.3–0.6 mJ for 2–3-nm-thick SAFs. On the other hand, the upper bound of $\Delta\gamma_{\text{eq.}}$ ($T > 900$ °C) is calculated from the measured advancing contact angle to be ~ 1 mJ (Fig. 10c) and the lower bound of $\Delta\gamma_{\text{eq.}}$ (1050 °C) is calculated to be ~ 0.5 mJ by estimating the receding contact angle (using Eqs. (15) and (16)). This experimentally obtained range of $\Delta\gamma_{\text{eq.}}$ (0.5–1 mJ) is consistent with the theoretical estimation of 0.3–0.6 mJ for 2–3-nm-thick SAFs.

Alternatively, Eqs. (24) and (26) can be combined to directly estimate the “residual” contact angle, which is computed to be $\sim 5.5^\circ$ for a 2-nm-thick SAF or $\sim 3.6^\circ$ for a 3-nm-thick SAF. This estimation again agrees well with experimental observations ($4^\circ < \theta_Y < 6^\circ$; see Eq. (16)). Therefore, the quantitative agreement supports the interpretation that complete wetting is inhibited by the long-range attractive dispersion force.

5. Conclusions

Anisotropic wetting of Bi_2O_3 -rich liquid on ZnO single crystals of different orientations is correlated with anisotropic SAF formation. The measured contact angle decreases monotonically with increasing temperature from 740 to ~ 860 °C on the $\{11\bar{2}0\}$ surfaces where nanometer-thick SAFs are present in equilibrium with partial-wetting drops, while the contact angle is virtually constant on $\{1\bar{1}00\}$ surfaces where SAFs are not present. Furthermore, a crossover in contact angle vs. temperature is observed on the $\{11\bar{2}0\}$ surface where the advancing contact angle becomes constant at $\sim 6^\circ$ above ~ 860 °C. Analysis of two-stage isothermal drop receding kinetics show that complete wetting does not occur up to 1050 °C. The receding contact angle, or the lower bound of the Young contact angle, is $\sim 4^\circ$. The effects of faceted ridges forming at the triple lines have been observed and taken into account in analyzing the results.

The observed contact angle’s dependence on temperature supports a generalized Cahn model for wetting in the presence of nanoscale SAFs, where the SAFs thicken with increasing temperature due to entropic interactions. Furthermore, the presence of an attractive London dispersion force of significant strength should extend the stability regime for nanoscale SAFs to higher temperatures, delaying or prohibiting the onset of complete wetting. While the formation of faceted ridges at triple lines results in a significant pinning effect for drop advancement (or reced-

ing), the complete wetting transition predicted from the basic Cahn wetting model is inhibited by the attractive, long-range dispersion force. Quantification of a simplified thermodynamic model shows that the experimentally observed “residual” contact angle of $\sim 4\text{--}6^\circ$ can be explained from the magnitude of the attractive dispersion force. It is expected that similar models and phenomena apply to wetting at grain boundaries in the presence of nanoscale intergranular films, where the dispersion forces are always attractive, but often weaker than those for SAFs.

Acknowledgements

This work is supported by an NSF CAREER award (DMR-0448879, to J.L. and H.Q.). Y.-M. C. acknowledges support by NSF/EU NANOAM collaboration (NSF DMR-0010062, EUG5RD-CT-2001-00586), and NSF Grant No. CMS-0609050. We thank Ming Tang for his useful comments regarding the wetting transitions. J.L. and Y.M.C. gratefully acknowledge the late Dr. Rowland M. Cannon (1943–2006) for his many deep insights and for his continuing inspiration and support over many years.

References

- [1] Clarke DR. *J Am Ceram Soc* 1987;70:15.
- [2] Cannon RM, Esposito L. *Z Metallkd* 1999;90:1002.
- [3] Cannon RM, Rühle M, Hoffmann MJ, French RH, Gu H, Tomsia AP, et al. Adsorption and wetting mechanisms at ceramic grain boundaries. In: Sakuma T, Ikuhara Y, editors. *Grain boundary engineering in ceramics*, vol. 118. The American Ceramic Society; 2000. p. 427.
- [4] Subramaniam A, Koch CT, Cannon RM, Rühle M. *Mater Sci Eng A* 2006;422:3.
- [5] Avishai A, Scheu C, Kaplan WD. *Acta Mater* 2005;53:1559.
- [6] Scheu C, Dehm G, Kaplan WD. *J Am Ceram Soc* 2000;84:623.
- [7] Avishai A, Kaplan WD. *Z Metallkd* 2004;95:266.
- [8] Avishai A, Scheu C, Kaplan WD. *Z Metallkd* 2003;94:272.
- [9] Baram M, Kaplan WD. *J Mater Sci* 2006;41:7775.
- [10] Jeong HG, Hiraga K, Mabuchi M, Higashi K. *Philos Mag Lett* 1996;74:73.
- [11] Luo J, Gupta VK, Yoon DH, Meyer HM. *Appl Phys Lett* 2005;87:231902.
- [12] Gupta VK, Yoon DH, Meyer III HM, Luo J. *Acta Mater* 2007;55:3131.
- [13] Luo J, Chiang Y-M. *J Eur Ceram Soc* 1999;19:697.
- [14] Luo J, Chiang Y-M. *Acta Mater* 2000;48:4501.
- [15] Luo J, Chiang Y-M, Cannon RM. *Langmuir* 2005;21:7358.
- [16] Luo J, Tang M, Cannon RM, Carter WC, Chiang Y-M. *Mater Sci Eng A* 2006;422:19.
- [17] Qian H, Luo J. *Appl Phys Lett* 2007;91:061909.
- [18] Luo J. *Crit Rev Solid State Mater Sci* 2007;32:67.
- [19] Tang M, Carter WC, Cannon RM. *Phys Rev Lett* 2006;97:075502.
- [20] Cahn JW. *J Chem Phys* 1977;66:3667.
- [21] Dash JG. *Contemp Phys* 1989;30:89.
- [22] Dash JG, Fu H, Wettlaufer JS. *Rep Prog Phys* 1995;58:115.
- [23] Dash JG, Rempel AM, Wettlaufer JS. *Rev Mod Phys* 2006;78:695.
- [24] Brochard-Wyart F, di Meglio J-M, Quéré D, de Gennes PG. *Langmuir* 1991;7:335.
- [25] de Gennes PG. *Rev Mod Phys* 1985;57:827.
- [26] Bertrand E, Dobbs H, Broseta D, Indekeu J, Bonn D, Meunier J. *Phys Rev Lett* 2000;85:1282.
- [27] Cheng W-C, Chatain D, Wynblatt P. *Surf Sci* 1995;327:501.
- [28] Chatain D, Metois JJ. *Surf Sci* 1993;291:1.
- [29] Luo J, Qian H, Shi X. Interface stabilized nanometer-thick disordered films. In: Nalwa HS, editor. *Encyclopedia of nanoscience and nanotechnology*, 2nd ed. Valencia (CA): American Scientific Publishers, in press.
- [30] Dietrich S. Wetting phenomena. In: Domb C, Lebowitz JL, editors. *Phase transitions and critical phenomena*, vol. 12. London: Academic Press; 1988. p. 1.
- [31] Lipowsky R. *Phys Rev Lett* 1986;57:2876.
- [32] Gambino JP. *J Am Ceram Soc* 1989;72:642.
- [33] Chiang Y-M, Ramos A, Tang M. Unpublished results, 2004.
- [34] Wang H, Chiang Y-M. *J Am Ceram Soc* 1998;81:89.
- [35] Chiang Y-M, Wang H, Lee J-R. *J Microscopy* 1998;191:275.
- [36] Lee J-R, Chiang Y-M, Ceder G. *Acta Mater* 1997;45:1247.
- [37] Safronov GM, Batog VN, Stepanyuk TV, Fedorov PM. *Russ J Inorg Chem* 1971;16:460.
- [38] Saiz E, Cannon RM, Tomsia AP. *Acta Mater* 2000;48:4449.
- [39] Saiz E, Tomsia AP, Cannon RM. *Acta Mater* 1998;46:2349.
- [40] Saiz E, Tomsia AP, Cannon RM. *Script Mater* 2001;44:159.
- [41] Ghetta V, Chatain D. *J Am Ceram Soc* 2002;85:961.
- [42] Israelachvili JN. *Intermolecular and surface forces*. London: Academic Press Limited; 1994.
- [43] Bonn D, Ross D. *Rep Prog Phys* 2001;64:1085.
- [44] Samsonov GV. *The oxide handbook*. New York: Plenum Data Company; 1982.
- [45] French RH. *J Am Ceram Soc* 2000;83:2117.